

Large-Scale Synthesis of Colloidal Fe_3O_4 Nanoparticles Exhibiting High Heating Efficiency in Magnetic Hyperthermia

Yury V. Kolen'ko,^{*,†} Manuel Bañobre-López,[†] Carlos Rodríguez-Abreu,[†] Enrique Carbó-Argibay,[†] Alexandra Sailsman,[‡] Yolanda Piñeiro-Redondo,[#] M. Fátima Cerqueira,[§] Dmitri Y. Petrovykh,[†] Kirill Kovnir,[⊥] Oleg I. Lebedev,^{||} and José Rivas[†]

[†]International Iberian Nanotechnology Laboratory, Braga 4715-330, Portugal

[‡]Department of Materials Science and Engineering, Massachusetts Institute of Technology, Cambridge Massachusetts 02139, United States

[#]Department of Applied Physics, University of Santiago de Compostela, Santiago de Compostela 15782, Spain

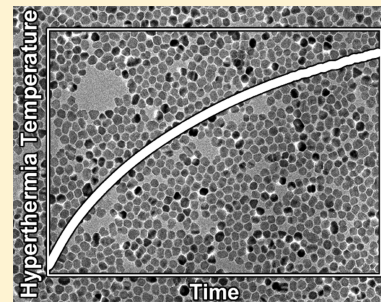
[§]Center of Physics, University of Minho, Braga 4710-057, Portugal

[⊥]Department of Chemistry, University of California, Davis, Davis, California 95616, United States

^{||}CRISMAT, UMR 6508, CNRS-ENSICAEN, Caen 14050, France

S Supporting Information

ABSTRACT: Exceptional magnetic properties of magnetite, Fe_3O_4 , nanoparticles make them one of the most intensively studied inorganic nanomaterials for biomedical applications. We report successful gram-scale syntheses, via hydrothermal route or controlled coprecipitation in an automated reactor, of colloidal Fe_3O_4 nanoparticles with sizes of 12.9 ± 5.9 , 17.9 ± 4.4 , and 19.8 ± 3.2 nm. To investigate structure–property relationships as a function of the synthetic procedure, we used multiple techniques to characterize the structure, phase composition, and magnetic behavior of these nanoparticles. For the iron oxide cores of these nanoparticles, powder X-ray diffraction and electron microscopy both confirm single-phase Fe_3O_4 composition. In addition to the core composition, the magnetic performance of nanoparticles in the 13–20 nm size range can be strongly influenced by the surface properties, which we analyzed by three complementary techniques. Raman scattering and X-ray photoelectron spectroscopy (XPS) measurements indicate overoxidation of nanoparticle surfaces, while transmission electron microscopy (TEM) shows no distinct core–shell structure. Considered together, Raman, XPS, and TEM observations suggest that our nanoparticles have a gradually varying nonstoichiometric $\text{Fe}_3\text{O}_{4+\delta}$ composition, which could be attributed to the formation of Fe_3O_4 – γ - Fe_2O_3 solid solutions at their outermost surface. Detailed analyses by TEM reveal that the hydrothermally produced samples include single-domain nanocrystals coexisting with defective twinned and dimer nanoparticles, which form as a result of oriented-attachment crystal growth. All our nanoparticles exhibit superparamagnetic-like behavior with a characteristic blocking temperature above room temperature. We attribute the estimated saturation magnetization values up to 84.01 ± 0.25 emu/g at 300 K to the relatively large size of the nanoparticles (13–20 nm) coupled with the syntheses under elevated temperature; alternative explanations, such as surface-mediated effects, are not supported by our spectroscopy or microscopy measurements. For these colloids, the heating efficiency in magnetic hyperthermia correlates with their saturation magnetization, making them appealing for therapeutic and other biomedical applications that rely on high-performance nanoparticle-mediated hyperthermia.



1. INTRODUCTION

Naturally ferrimagnetic (FiM) magnetite, Fe_3O_4 , with a multidomain magnetic structure is an iron oxide polymorph appealing for a variety of applications because bulk Fe_3O_4 exhibits a high Curie temperature ($T_C^{\text{bulk}} = 840$ K) and the highest saturation magnetization ($M_s^{\text{bulk}} = 98$ emu/g) among iron oxides.¹ In nanoparticle (NP) form, the magnetic behavior of Fe_3O_4 is predominantly determined by the size of the particles. FiM Fe_3O_4 NPs undergo a transition from multi- to single-domain magnetic structure as their size is reduced below 80–90 nm.² Upon further size reduction to 25–30 nm, Fe_3O_4 NPs turn into superparamagnetic (SPM) state at room

temperature (RT) as a consequence of the spontaneous flip of their magnetization (M), which is determined by the balance between thermal energy and magnetic anisotropy.² SPM NPs are particularly desirable for preparing colloidally stable dispersions because larger (≥ 25 –30 nm) FiM NPs exhibit remanence and coercive forces that cause aggregation under a magnetic field. Colloidally stable SPM NPs exhibit a high M_s , good chemical stability,¹ biocompatibility,³ and low toxicity,⁴

Received: January 23, 2014

Revised: April 1, 2014

Published: April 2, 2014



therefore, they are one of the benchmark nanomaterials for a diverse range of practical applications, including magnetic resonance imaging, NP-mediated magnetic hyperthermia, separation, catalysis, drug delivery, and water purification.⁵ Optimizing SPM Fe₃O₄ NPs for specific applications requires improvements in two critical areas: (1) synthesis of NPs having a large size (around 20 nm) and relatively narrow size distribution, and (2) elucidation of their structure and phase composition to determine structure–property relationships.

A narrow particle size distribution around 20 nm maximizes M_s while reducing the undesirable FIM contribution of large NPs, which increases with polydispersity. The majority of the methods used to prepare Fe₃O₄ NPs lead to particle sizes of about 10 nm and to correspondingly low M_s values, following the general particle-size dependence of M_s .⁶ In contrast, M_s values as high as 85 emu/g (at 2 K) have been achieved for larger (20 nm) NPs;⁷ gram-scale synthesis of such large NPs, however, is difficult.⁸ Large colloidal SPM Fe₃O₄ NPs have been prepared mainly by three routes: (1) thermal decomposition,⁹ (2) mild oxidation of Fe²⁺ precursor¹⁰ followed by stabilization of the resultant NPs in colloidal form,¹¹ and (3) the classical synthesis of 10 nm NPs by coprecipitation followed by hydrothermal growth of the particles.¹² The limited number of the available synthesis methods provides a motivation for developing new protocols to prepare large SPM Fe₃O₄ NPs.

The structure and phase composition of colloidal SPM Fe₃O₄ NPs remain puzzling despite the availability of increasing amounts of structural information. Various spectroscopic measurements have shown that the structure of SPM Fe₃O₄ NPs can be described as a magnetite core with a thin overoxidized (Fe³⁺) surface shell, which is compositionally close to a maghemite polymorph (γ -Fe₂O₃).^{9a,12,13} Conversely, the putative Fe₃O₄@ γ -Fe₂O₃ core–shell structure has not been observed by X-ray diffraction or electron microscopy studies, supporting smooth nonstoichiometric Fe₃O_{4+ δ} formulation of magnetite NPs.¹⁴ This is most likely attributed to the topotactic oxidation of Fe₃O₄ surface with the formation of solid solution Fe₃O₄– γ -Fe₂O₃.¹⁵

Unambiguous determination of the structure and phase composition of SPM Fe₃O₄ NPs is important because these parameters dramatically affect the M_s values. For instance, improved purity and crystallinity of colloidal SPM Fe₃O₄ NPs produced at elevated temperatures are believed to be responsible for their enhanced M_s (70–85 emu/g),^{7,9} thus both bulk and surface composition information may be pertinent for elucidating the structure–property relationships for NPs. The capping ligand is another surface-based factor thought to be capable of enhancing M_s .^{7,16} A better understanding of how the structure and phase composition of Fe₃O₄ NPs depend on their synthesis is thus necessary for a more precise control over their magnetic properties.

Magnetic properties of nanoparticles determine their performance in magnetic hyperthermia, a process of heating SPM NPs by magnetization reversal effects induced under exposure to an external oscillating magnetic field. Hyperthermia induced in SPM NPs can be used, for example, to locally heat and thus destroy cancer cells.¹⁷ The mechanism of magnetic hyperthermia is not fully understood, despite multiple previous theoretical and experimental studies. Rosensweig developed the first theoretical approach, in which the specific absorption rate (SAR) produced by hyperthermia in diluted SPM ferrofluids is attributed to Néel and Brown relaxation processes, while for particles \geq 25 nm in size, ferromagnetic or FIM heat release is

ascribed to hysteresis losses.¹⁸ This separation of relaxation and hysteresis losses has been subsequently criticized by Carrey and co-workers, who proposed a more comprehensive theoretical framework that combined Stoner–Wohlfarth-based theories, linear response theories, and equilibrium functions, intending to explain the SAR produced by magnetic NPs of any size.¹⁹ Later, Vallejo-Fernandez and co-workers concluded that the susceptibility losses are negligible and the heat is mostly generated by hysteresis loss.²⁰ Despite the large amount of SAR data found in the literature, none of the models have been clearly confirmed experimentally due to complex contributions of the colloidal parameters, such as anisotropy constant, particle volume, viscosity of the medium, involved in magnetic hyperthermia mechanisms.

In this paper, we outline new and improved large-scale routes to highly crystalline hydrophilic and hydrophobic SPM Fe₃O₄ NPs having mean particle size as large as 20 nm and exhibiting room temperature M_s as high as 84 emu/g. We analyze the structure and phase composition of synthesized SPM Fe₃O₄ NPs by several complementary bulk- and surface-sensitive techniques. We observe that the synthesized NPs have a single-phase magnetite structure with an overoxidized surface, although no distinct core–shell nanostructure appears to be present. Furthermore, we show that hydrothermally prepared NPs can exhibit dimer-like or twinned internal structure formed by oriented attachment crystal growth. Finally, we demonstrate that the synthesized colloidal NPs not only show superparamagnetic behavior with notably high saturation magnetization, but also exhibit excellent performance in magnetic hyperthermia.

2. EXPERIMENTAL SECTION

Large-Scale Synthesis of Hydrophilic NPs by Coprecipitation. Hydrophilic Fe₃O₄ NPs were synthesized on a large scale by controlled coprecipitation in an automated batch reactor Atlas Potassium (Syrris), equipped with two syringe pumps (Syrris), temperature control system LH85 PLUS (Julabo), overhead stirrer, as well as temperature, pH, and turbidity probes. Briefly, 40.75 mmol of FeCl₂·4H₂O (99%, Sigma-Aldrich) and 74 mmol of FeCl₃·6H₂O (99%, Sigma-Aldrich) were dissolved in a 2 L glass reaction vessel filled with 1.1 L of ultrapure water (produced by Milli-Q Advantage A10 system, Millipore) to obtain a clear orange solution. The solution was heated to 363 K and then 60 mL of aqueous ammonia solution (28–30%, Sigma-Aldrich) was added at 10 mL/min with the use of a syringe pump. Next, the resultant black slurry was left at 363 K for 10 min and then 100 mL of aqueous solution containing 12 g of poly(acrylic acid sodium salt) ($M_w \approx 5100$, Sigma-Aldrich) was added at 10 mL/min with use of a second syringe pump. The system was then aged at 363 K for 1 h and, finally, cooled to ambient temperature. All the aforementioned procedures were performed under constant stirring at 300 rpm. A typical time log of the preparation in the automated reactor is given in Figure S1 in the Supporting Information (SI).

Fe₃O₄ NPs were collected by a NdFeB magnet and redispersed in water by using a propeller VOS 14 stirrer (VWR) and ultrasonic treatment in a S-250D sonifier (Branson). To remove any unbound poly(acrylic acid) (PAA), the water-dispersed NPs were centrifuged at 20 000 rpm for 15 min with an Allegra 64R centrifuge (Beckman Coulter), and washed. This purification procedure was repeated twice, and the resultant NPs were redispersed in water and

Table 1. Average Particle Diameter, Phase Composition, and Lattice Parameters of the Synthesized NPs

sample	synthesis method	capping ligand	DLS mean hydrodynamic diameter (nm)	DLS polydispersity index	TEM average diameter (nm) ^a	XRD and TEM phase composition	unit cell parameter <i>a</i> (Å)	Raman local structure
PAA-CP	coprecipitation 363 K, 1 h	PAA	112.2	0.44	12.9 ± 5.9	Fe ₃ O ₄	8.362(1)	Fe ₃ O ₄ + γ -Fe ₂ O ₃ ^b
PAA-HT	hydrothermal 473 K, 24 h	PAA	94.8	0.36	17.9 ± 4.4	Fe ₃ O ₄	8.3558(7)	Fe ₃ O ₄ + γ -Fe ₂ O ₃ ^b
OL-HT	hydrothermal 473 K, 24 h	OL	33.9	0.41	19.8 ± 3.2	Fe ₃ O ₄	8.356(2)	Fe ₃ O ₄ + γ -Fe ₂ O ₃

^aEstimated with use of ImageJ software. ^bMinor admixture of the γ -Fe₂O₃ phase.

centrifuged at 3 000 rpm for 10 min to remove any insoluble solids. Finally, the NPs were stored in water. The surface of thus synthesized NPs is passivated with hydrophilic PAA, which provides enough free carboxyl groups (noncoordinated to the surface of the NPs) for long-term colloidal stabilization by electrostatic repulsion forces. The yield of colloidal PAA-coated Fe₃O₄ NPs synthesized by coprecipitation (PAA-CP) in the automated reactor was established to be 68% (\approx 6.5 g).

Synthesis of Hydrophilic NPs by the Hydrothermal Method. Hydrophilic Fe₃O₄ NPs were synthesized using a novel hydrothermal method. Briefly, 8 mmol of FeCl₂·4H₂O and 14 mmol of FeCl₃·6H₂O were dissolved in a 40 mL poly(tetrafluoroethylene) (PTFE) vessel filled with 7 mL of water (deoxygenated via N₂ bubbling prior to use). Next, 15 mL of aqueous ammonia solution was added, and subsequently 2 g of poly(acrylic acid sodium salt) in 5 mL of water was rapidly added to the reaction mixture. The PTFE vessel with the resultant black suspension was capped and placed into a stainless steel autoclave. The autoclave was sealed and kept at 473 K for 24 h under autogenous pressure.

Fe₃O₄ NPs were precipitated from the resultant product mixture by adding acetone (99.5%, Sigma-Aldrich), followed by centrifugation at 9 000 rpm for 10 min. The NPs were redispersed in water, and centrifuged at 20 000 rpm for 1.5 h to remove unbound PAA. This purification procedure was repeated. To separate any non-dispersible solids, the resultant NPs were redispersed in water and centrifuged at 3 000 rpm for 10 min, and finally stored in water. The yield of colloidal PAA-coated Fe₃O₄ NPs synthesized by the hydrothermal method (PAA-HT) was estimated to be 86% (\approx 1.4 g).

Synthesis of Hydrophobic NPs by the Hydrothermal Method. Hydrophobic Fe₃O₄ NPs were prepared by a modified hydrothermal approach adapted from that of Taniguchi and co-workers.^{14a} The synthesis proceeded by dissolution of 8 mmol of FeCl₂·4H₂O and 14 mmol of FeCl₃·6H₂O in a 40 mL PTFE vessel filled with 7 mL of deoxygenated water. In parallel, 1.64 mmol of sodium oleate (82%, Sigma-Aldrich) was dissolved in 5 mL of water at 333 K. This solution was added to the Fe-containing one, and 15 mL of aqueous ammonia solution was subsequently added, turning the suspension black. The PTFE vessel was capped and placed into a stainless steel autoclave, then the autoclave was sealed, and kept at 473 K for 24 h under autogenous pressure.

The black product of the hydrothermal synthesis was collected by decantation, washed twice with water by using propeller stirring and ultrasonic processing, isolated via centrifugation at 20 000 rpm for 30 min (after first washing) and 1 h (after second washing), and dried overnight under vacuum at RT. The resulting product was then redispersed in cyclohexane (99.8%, Sigma-Aldrich) and centrifuged at 3 000 rpm for 10 min to remove any insoluble solids. To remove

unbound oleate (OL) ligands, ethanol was added to precipitate the NPs, followed by centrifugation at 6 000 rpm for 10 min and further redispersion in cyclohexane. After repeating this procedure twice, the NPs were stored in cyclohexane. The surface of as-prepared OL-coated NPs is hydrophobic due to the long alkyl chains from the fatty OL ligands. This enables the NPs to be readily dispersed in nonpolar solvents, generating samples that are colloidally stable for months. The yield of colloidal OL-coated Fe₃O₄ NPs synthesized by the hydrothermal method (OL-HT) was calculated to be 68% (\approx 0.9 g).

Characterization. The products were characterized by transmission electron microscopy (TEM), electron diffraction (ED) and high-resolution TEM (HRTEM) (Tecnai G² 30 UT and Titan ChemiSTEM microscopes, FEI Company), dynamic light scattering (DLS) (SZ-100 nanoparticle analyzer, Horiba), powder X-ray diffraction (XRD) (X'Pert PRO diffractometer, PANalytical),²¹ Raman scattering (alpha300 R confocal Raman microscope, WITec), X-ray photoelectron spectroscopy (XPS) (ESCALAB 250Xi, Thermo Scientific),²² thermogravimetry and differential scanning calorimetry coupled to online mass spectrometry (TGA-DSC-MS) (TGA/DSC 1 STAR^c system, Mettler-Toledo, fitted with OmniStar GSD320 gas analysis system, Pfeiffer Vacuum), colloidal stability testing, vibrating sample magnetometry (VSM) (EV9, Lot-Oriel), magnetization measurements (SQUID-VSM magnetometer, Quantum Design), and magnetic hyperthermia measurements (DM 100 system, nB nanoScale Biomagnetics). The detailed descriptions of NP characterization are presented in the SI.

3. RESULTS

Synthesis. To obtain SPM NPs of up to 20 nm in size, we were particularly interested in the synthesis at elevated temperatures. Through controlled coprecipitation via an automated reactor, we were able to synthesize about 6.5 g of colloidal Fe₃O₄ NPs in one batch. The initial stage of this approach involves the coprecipitation of Fe²⁺ and Fe³⁺ at elevated temperature to generate nanocrystalline magnetite, which is subsequently functionalized by PAA to provide water-dispersible NPs (PAA-CP). To optimize phase purity, colloidal stability, magnetic performance, and yield of Fe₃O₄ NPs with the desired large size, we explored a range of reaction conditions (temperature: 283–363 K; duration: 1–24 h). Our analysis of the produced samples reveals that the synthesis at 363 K for 1 h (Figure S1, SI) gave the best result among the explored conditions, providing optimal colloidal Fe₃O₄ NPs in 68% yield. We find that long reaction time results in partially overoxidized products, such as γ -Fe₂O₃, with decreased M_s (50–55 emu/g), whereas lower temperatures lead to colloids with reduced M_s (40–55 emu/g).

We have also synthesized Fe₃O₄ colloids following the hydrothermal route, with considerably different yields com-

pared to the reported procedure.^{14a} In particular, three times the amount of starting materials and optimized quantities of capping agent were applied to increase the quality and yield of the colloids. Additionally, we increased the temperature to 473 K and duration of the hydrothermal treatment to 24 h, thereby improving shape and size uniformity of the NPs. Functionalization of the particles with PAA and OL ligands in the course of hydrothermal synthesis provided stable hydrophilic (**PAA-HT**) and hydrophobic (**OL-HT**) Fe_3O_4 colloids in 86% and 68% yield, respectively.

NP Sizing and Microstructure. To provide insight into the size, morphology, and any structural defects of the synthesized colloidal Fe_3O_4 NPs, we carried out a detailed TEM investigation. Low-magnification TEM images indicate that the synthesized and purified samples consist of faceted NPs and the average diameters of primary particles are 13 ± 6 , 18 ± 4 , and 20 ± 3 nm for **PAA-CP**, **PAA-HT**, and **OL-HT**, respectively (Table 1, Figure 1). The ED patterns also reveal an overall high degree of crystallinity and structural homogeneity of the Fe_3O_4 NPs. The ED ring patterns can be completely indexed based on magnetite structure in the cubic $Fd\bar{3}m$ space group using the unit cell parameters determined by XRD (Table 1). No rings associated with secondary phases or amorphous structures have been detected.

We note that the mean size of PAA-coated particles estimated by DLS is 5–8 times higher than that measured by TEM (Table 1). This discrepancy can be attributed to clustering of NPs in solution, which has been reported previously for NPs coated with low molecular weight PAA.¹¹ This clustering, however, is apparently self-limiting in our colloids, as it does not proceed beyond small clusters and thus does not produce colloidal instability or sedimentation, as further discussed in a dedicated section. In TEM images, any such small NP clusters formed in the colloidal solution are difficult to observe unambiguously, because the observed clustering of NPs in TEM images (e.g., in Figure 1) is dominated by the effects of drying that colloidal solution on top of a TEM grid.

HRTEM and Structural Defects. HRTEM images and Fourier-transform (FT) patterns of the NPs from PAA- and OL-coated samples (Figures 2 and 3) confirm that NPs are single-phase magnetite, devoid of other impurity phases or a distinct core–shell structure, unlike that observed for other iron oxide NPs.^{9a,12,13} For all particles, the main surface planes are of {111} type, i.e., crystal planes with low surface energy.

All NPs can be divided into three general groups based on the structural perfection observed in HRTEM images: structural-defect-free NPs, twinned NPs, and “dimer” NPs. While the **PAA-CP** NPs exhibit a clear faceting structure (Figure 2a), the NPs in both hydrothermally produced samples exhibit more round shapes (Figures 2b and 3a). Only the hydrothermally produced samples feature bright-contrast boundaries dividing NPs that comprise two isostructural parts; we denote this type of Fe_3O_4 particles “dimer” NPs. Figures 2b and 3a show HRTEM images of a dimer nanoparticle and a similar boundary along the [011] and [211] direction, respectively.

To clarify the nature of such defects, HRTEM images have been subjected to geometric phase analysis (GPA), a powerful method for strain mapping from HRTEM images²³ that produces a map of shift and rotation of lattice planes in a “temperature” color scale. As is typical for twinning planes in cubic structures (Figure 3b), the boundary plane in Figure 2b is

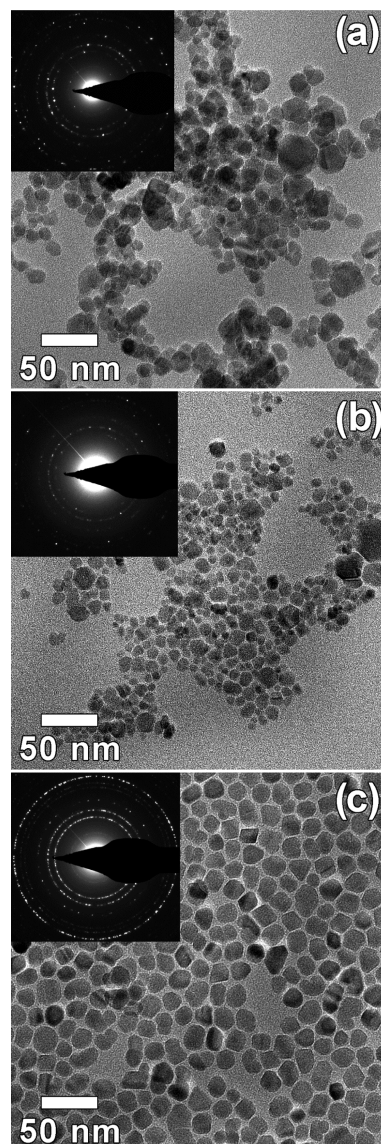


Figure 1. Low-resolution bright-field TEM images and corresponding ED ring patterns of three Fe_3O_4 NP samples synthesized under different conditions: (a) PAA-coated Fe_3O_4 prepared by coprecipitation. (b) PAA- and (c) OL-coated Fe_3O_4 synthesized by hydrothermal route.

of {111} type. We did not find, however, any shift or rotation of the lattice planes across the boundary (top inset in Figure 2b), ruling out its assignment as a twin or antiphase boundary. FT and GPA confirm identical structure and orientation for both parts of the dimer Fe_3O_4 NPs. The GPA results are presented for two selected Fe_3O_4 NPs (imaged along [011] and [211] orientations) in the insets of Figures 2b and 3a, respectively. There is no lattice distortion along any of the out-of-plane boundary directions, resulting in uniform GPA color mapping of NPs along $g\bar{0}11$ in Figure 2b and $g0\bar{1}\bar{1}$ in Figure 3a. In contrast, GPA images along the boundary plane direction ($g1\bar{1}1$ in Figure 2b and $g\bar{1}11$ in Figure 3a) show a pronounced divergence in the bulk color of the nanoparticle material at the boundary line. These GPA data strongly suggest differences in the distances of two successive planes at the boundary, which can be associated with a stacking-fault defect. The inset in Figure 2b shows the structural model of such a dimer boundary.

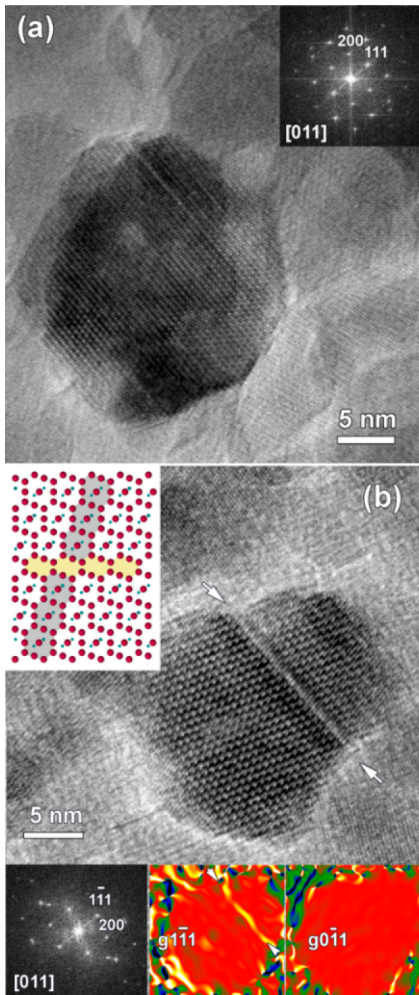


Figure 2. Bright-field [011] HRTEM images of PAA-coated Fe_3O_4 NPs synthesized by coprecipitation (a) and the hydrothermal method (b). FT patterns are shown in the top-right (a) and bottom-left (b) insets. White arrows in part b mark the boundary within a dimer NP; a structural model of this interface is shown in the top-left inset: Fe atoms = red, O atoms = blue, $\{111\}$ -type planes = gray background, dimer boundary = yellow background. The $g\bar{1}\bar{1}1$ and $g0\bar{1}\bar{1}$ GPA images of the dimer NP in part b are shown in the bottom-right insets.

This model, which was directly picked up from [011] HRTEM images, clearly indicates that the dimer boundary has a structure distinct from that of bulk Fe_3O_4 .

For comparison with dimer NPs, Figure 3b depicts a typical twinned NP imaged along [110] zone axis orientation. As expected, the twinned NP is significantly different from dimer NPs in terms of structure. In particular, there is a clear flipping of Fe_3O_4 structure around the $\{111\}$ twin plane. Small distortion notwithstanding, the structure of the twin plane and the structure of magnetite are closely related (inset in Figure 3b).

Crystal Structure and Chemical Composition. Understanding the material properties of iron oxide NPs is critical for evaluating their quality and suitability for specific applications. We employed several complementary methods to characterize the phase and chemical composition of the iron oxide component of our NPs.

XRD. All samples exhibited very similar XRD patterns (Figure 4) characterized by high background and broad peaks, which are typical of nanocrystalline powders. According to the

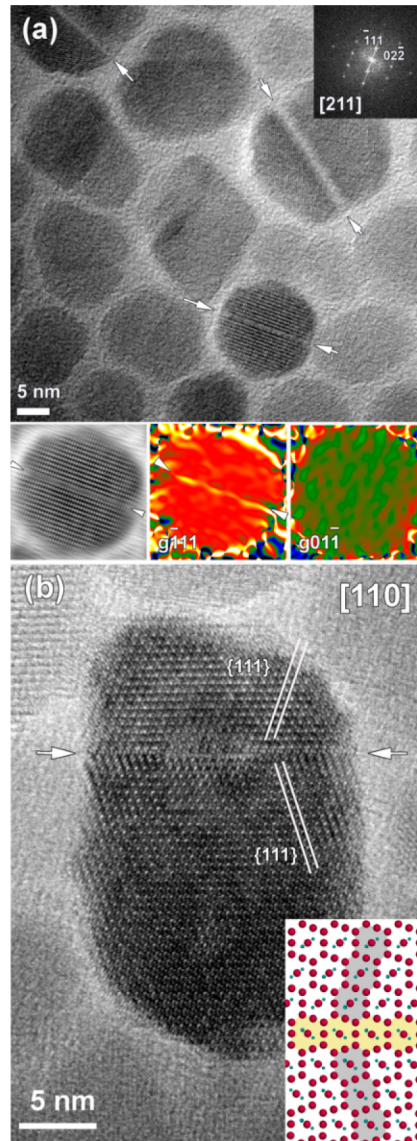


Figure 3. (a) Representative HRTEM image together with FT pattern (inset) of OL-coated Fe_3O_4 NPs prepared by the hydrothermal method. White arrows mark the dimer boundaries. Bottom insets: a filtered HRTEM image of a selected dimer NP (left) and the corresponding GPA images for $g\bar{1}\bar{1}1$ (middle) and $g0\bar{1}\bar{1}$ (right) diffraction spots. (b) HRTEM image of a twinned NP in the hydrothermal sample and the corresponding structural model (Fe atoms = red, O atoms = blue). A single $\{111\}$ -type twinning plane (indicated by white arrows in the image and yellow background in the model) is imaged along the [110] zone axis. White parallel lines in the image and gray background stripes in the model depict other $\{111\}$ planes located in each of the twinned parts of this NP.

phase analysis, all products are phase-pure cubic Fe_3O_4 , in good agreement with ED results from TEM characterization. The cubic unit cell parameters a for different Fe_3O_4 NPs (Table 1) are in agreement with $a = 8.35 \text{ \AA}$, reported for the nanosized magnetite.²⁴ The two samples prepared by the hydrothermal method exhibit similar unit cells, while a slightly larger unit cell is found for the sample prepared by coprecipitation. This difference in the unit cell size indicates that different synthetic methods result in magnetite samples with slightly different stoichiometry or defect concentrations. We have specifically looked for but not detected any XRD peaks related to other

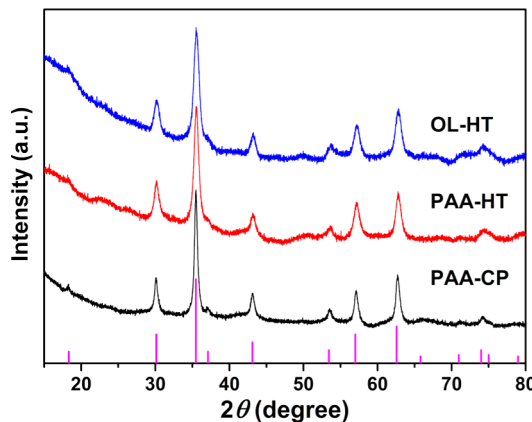


Figure 4. Powder XRD patterns of the synthesized NPs. Tick marks below the patterns correspond to the positions of the Bragg reflections expected for the magnetite phase.

crystalline phases, including the most likely admixtures, such as maghemite ($\gamma\text{-Fe}_2\text{O}_3$), hematite ($\alpha\text{-Fe}_2\text{O}_3$), or goethite ($\alpha\text{-FeOOH}$).

Raman Scattering. While XRD measures the average crystal symmetry of the samples, Raman scattering probes the structure of NPs localized within the Raman focal point. This technique can unambiguously detect the different oxide phases, because different iron oxide polymorphs show distinct Raman-active phonon modes.²⁵

Figure 5 shows typical Raman spectra measured on freshly prepared powdered specimens. All of the products exhibit

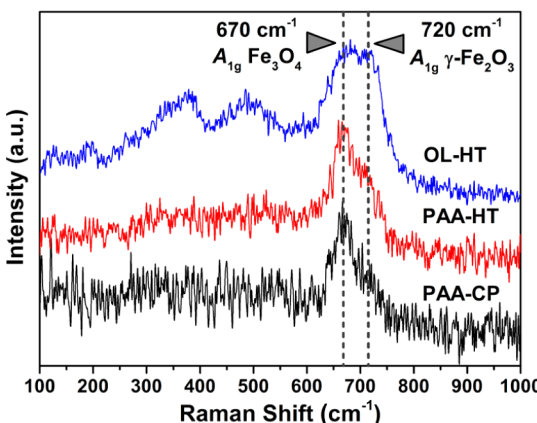


Figure 5. Raman scattering data for the synthesized NPs. Dashed lines denote the most intense A_{1g} modes of Fe_3O_4 and $\gamma\text{-Fe}_2\text{O}_3$.

spectra typical for nanopowders with broad peaks and low signal-to-noise ratio. The prominent band centered near 670 cm^{-1} is associated with the A_{1g} phonon mode of Fe_3O_4 with inverse-spinel crystal structure.^{25a} A shoulder observed in each spectrum at around 720 cm^{-1} corresponds to the A_{1g} phonon mode of $\gamma\text{-Fe}_2\text{O}_3$.^{25b} The peaks at $350\text{ (}T_{2g}\text{)}$ and $500\text{ cm}^{-1}\text{ (}E_g\text{)}$, though clearly observable only for OL-HT, are actually observed in all samples and correspond to the $\gamma\text{-Fe}_2\text{O}_3$ phase. The coexistence of Fe_3O_4 with an admixture of $\gamma\text{-Fe}_2\text{O}_3$ is clarified by fitting the Raman data for the hydrothermally derived NPs (Table S1 and Figure S2, SI). The $I(720)/I(670)$ intensity ratio increases from 0.18 to 0.33 and to 0.71 (Table S1, SI). The weak shoulder for PAA-coated NPs is an indication that these are largely composed of Fe_3O_4 . In contrast, the $\gamma\text{-}$

$\text{Fe}_2\text{O}_3\text{ A}_{1g}$ mode, together with two other characteristic bands for $\gamma\text{-Fe}_2\text{O}_3$ (T_{2g} and E_g), is more pronounced for OL-coated NPs, indicating that OL-HT NPs contain a larger concentration of $\gamma\text{-Fe}_2\text{O}_3$ than the PAA-coated NPs.

XPS. The oxidation state of iron at the outer surfaces of the synthesized NPs was further investigated by XPS. While the complex structure of these samples prevents us from performing a full quantitative deconvolution of the Fe 2p spectra,²⁶ the main $\text{Fe } 2p_{3/2}$ peak is observed at 710.3 eV binding energy (BE) for all three samples (Figure 6), which, together with the characteristic peak profile, indicates that the surface of the NPs is predominantly Fe^{3+} .²⁷

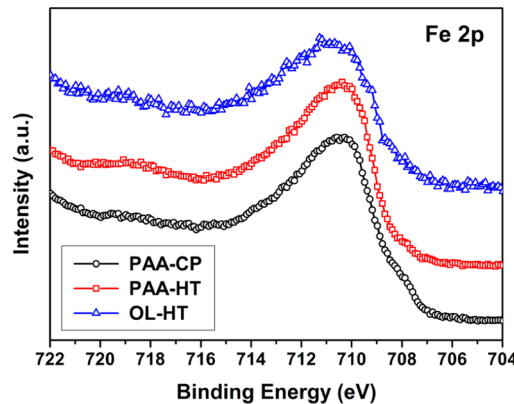


Figure 6. XPS characterization of the iron oxide states in the synthesized NPs. The main $\text{Fe } 2p_{3/2}$ peak is at 710.3 eV for all three samples; also present are weak satellites at 718.5 eV and shoulders at 708 eV.

A satellite feature at 718.5 eV is clearly observed for PAA-HT and in trace amounts for the other two samples; according to the literature, this satellite is most pronounced for pure Fe_2O_3 and is not observed for pure Fe_3O_4 .²⁸ Notably, this characteristic Fe^{3+} satellite is often associated with thermal treatment of iron oxide: it is typically observed for iron oxide NPs prepared by the hydrothermal methods^{27b} and can emerge upon heating a Fe_3O_4 film in synthetic dry air above 500 K.^{28c} A weak shoulder at 708 eV most likely corresponds to Fe^{2+} ; intensity in this BE range is commonly observed in iron oxide NPs and films.^{27,28c}

Protective Coating. We characterized the organic surface coatings of the NPs using two complementary methods: XPS and TGA-DSC-MS. XPS provides information about the stoichiometry of the organic shell, while TGA-DSC-MS is used to verify sample purity and evaluate thermal stability and transformations that occur at elevated temperature.

XPS. The XPS signals from PAA-coated samples are dominated by the iron oxide cores, while the signal from the OL-coated sample is dominated by the organic component, likely from the admixture of free OL chains that dried from solution together with NPs (Figure S3, SI).

Fitting reveals that the C 1s spectra of all the samples (top row in Figure 7) contain different ratios of three components: aliphatic C–C, carboxylic O=C=O, and ether (C–O–C) and/or alcohol (C–OH) C–O carbons.²⁹ While the presence of C–C and O=C=O species is expected for PAA and OL, the C–O chemistry most likely represents adventitious and/or solvent or precursor contamination. Both PAA-coated NPs, PAA-CP and PAA-HT, are similar in terms of C and O spectral

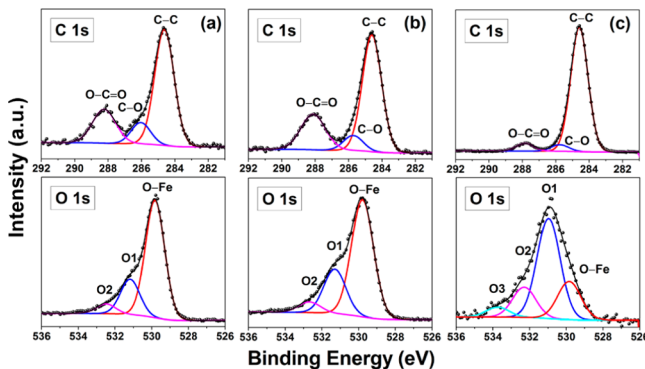


Figure 7. High-resolution XPS data in C 1s (top row) and O 1s (bottom row) regions for the PAA-coated NPs from coprecipitation (a), and PAA-coated (b) and OL-coated (c) NPs synthesized by the hydrothermal method.

components (Figure 7a,b), wherein the strongest O 1s component at 529.8 eV is from the iron oxide of the NP core.^{27b,28b,30} We detect roughly 50% more O in PAA-CP than the amount required to account for the O=C=O and C=O components in Figure 7a. O1 and O2 components can be produced by organic compounds or by water and hydroxyl,^{27b,28b,30} therefore, we believe that the PAA shell in PAA-CP is hydrated, which is further supported by TGA-DSC-MS analysis. For the OL-HT sample, the signal is dominated not by the OL shells of the NPs but by an OL overlayer of a few nanometers in thickness, as indicated by the strong inelastic background above Fe 2p peaks (Figure S3, SI). In the C 1s region, the C-C to O-C=O ratio of about 16 is close to what would be expected for (9Z)-octadec-9-enolate, OL, chains. The OL overlayer was presumably produced by mixing of secondary OL with the NPs during the specimen preparation for XPS analysis. We also note that the drying process inherently would dramatically concentrate any free OL from the initial NP stock dispersion, so detecting this amount of OL by XPS does not imply that the stock dispersion was heavily contaminated.

TGA-DSC-MS. To complement the XPS characterization, we also verified the presence of PAA and OL ligands on the NPs using TGA-DSC-MS. The TGA profiles (Figure S4, SI) exhibit stepwise weight-loss curves; the total weight losses between 303 and 1273 K in Ar are recorded to be 6.2%, 9.3%, and 15.0% for PAA-CP, PAA-HT, and OL-HT, respectively. The total weight loss consists of several main contributions: endothermic desorption of physically adsorbed water (up to 600 K), exothermic decomposition of organic capping agents (600–700 K), further degradation of the resultant carbonic residues (700–1000 K), and partial reduction of the Fe_3O_4 surface through reactions with C and H_2 (>1150 K). In particular, the presence and decomposition of the organic PAA and OL shells is confirmed by the intense peaks at m/z 44 (CO_2) in the MS ion curve between 600 and 1000 K. More details about the TGA-DSC-MS analysis are provided in the SI.

Colloidal Stability. The NP samples prepared in this work are stable against sedimentation when subjected to heating or moderate ionic strength and pH changes. Visual observations and DLS analysis (Table 1) of our Fe_3O_4 NPs confirm excellent dispersibility of the PAA-coated NPs in water and of the OL-coated NPs in nonpolar solvents. When heated to 363 K, none of the aqueous magnetite NP dispersions exhibit changes in color or sedimentation. In aqueous solutions of moderate ionic strength, dispersions of the PAA-HT colloid maintain

homogeneous color in the presence of up to 0.1 M NaCl (Figure S5b, SI); full precipitation is observed at 0.2 M NaCl concentration. In contrast, dispersions of the PAA-CP colloid begin aggregating at 0.04 M NaCl concentration and fully precipitate at 0.06 M NaCl (Figure S5a, SI).

Magnetic Properties. To fully characterize our Fe_3O_4 NPs, we analyzed their main magnetic properties: saturation magnetization, hysteresis, coercivity, anisotropy constant, and initial magnetic susceptibility (Table 2).

Table 2. Magnetic Properties of Colloidal Fe_3O_4 NPs

sample	PAA-CP	PAA-HT	OL-HT
M_s (emu/g(Fe_3O_4)) ^a	72.38 ± 0.19	84.01 ± 0.25	73.84 ± 0.21
H_C (Oe)	66.4	156.5	2.5
M_r (emu/g(Fe_3O_4))	1.3	3.2	0.3
K_{an} (emu/cm ³) ^b	32.3×10^5	37.5×10^5	37.0×10^5
χ_{in} ^c	0.128 ± 0.004	0.150 ± 0.006	0.0907 ± 0.0005
SAR (W/g) ^d	46.64	86.87	51.90
ILP (nH m ² /kg) ^e	1.09	2.03	1.21

^aEstimated by extrapolating M vs $1/H$ for $1/H \rightarrow 0$. ^bAnisotropy constant was calculated following the procedure of law of approach to saturation (LAS) for high fields.³¹ ^cInitial magnetic susceptibility at 300 K was calculated from $M(H)$ data as $\chi_{in} = (\partial M / \partial H)_{H \ll 1}$ for $H < 40$ (Oe). ^dSpecific absorption rates were calculated according to SAR = $(C_{sol}\rho_{sol}/\Phi)(\Delta T/\Delta t)$ ($V_{sol} = 1$ mL, $\Phi = 15$ g/L, $f = 300$ kHz, $H = 150$ Oe). ^eIntrinsic loss power (ILP) is a system independent parameter that allows direct comparison between different experimental setups (ILP = SAR/ H^2).³²

Magnetization. The magnetization versus magnetic field ($M(H)$) dependence at 300 K is shown in Figure 8a. All samples demonstrate SPM-like behavior exhibiting very high M_s values (Table 2); the PAA-HT sample shows highest M_s among the samples (Figure 8a). For the PAA-coated NPs, M_s exhibits the expected increase with increasing particle size, while the lowest M_s was observed for OL-coated NPs, despite those NPs having the largest size among the three samples. This low M_s likely results from the large number of structural and magnetic distortions at the surface of the OL-HT sample, as revealed by Raman scattering (Figure 5).

The anisotropy constants, K_{an} , for the NPs were estimated to be 32.3×10^5 – 37.5×10^5 emu/cm³ (Table 2), which is higher than that of bulk magnetite (1.2×10^5 emu/cm³). This K_{an} enhancement in nanoparticles is typically attributed to their high surface-to-volume ratio and correspondingly large contribution of the surface and shape anisotropy to overall K_{an} .

The low-field data (inset in Figure 8a) reveal small hysteresis loops characterized by low coercivity H_C (Table 2). At RT, OL-coated NPs exhibit the smallest coercivity (Table 2, inset in Figure 8a) despite having the largest diameter of the individual particles (TEM sizes in Table 1). This unexpected effect of size on coercive force is most likely explained by the dipolar magnetic interactions due to the clustering (i.e., aggregation) of smaller particles in both PAA-coated samples, as indicated by their hydrodynamic radii (Table 1).

Figure 8b displays the temperature dependence of magnetization ($M(T)$) for all three samples. From the zero-field-cooled (ZFC) and field-cooled (FC) curves, a strong magnetic dipolar particle interaction is clearly deduced: the FC curves are flat across the entire T range and the blocking temperatures (T_B) for all samples are well above 300 K. The 13–20 nm size

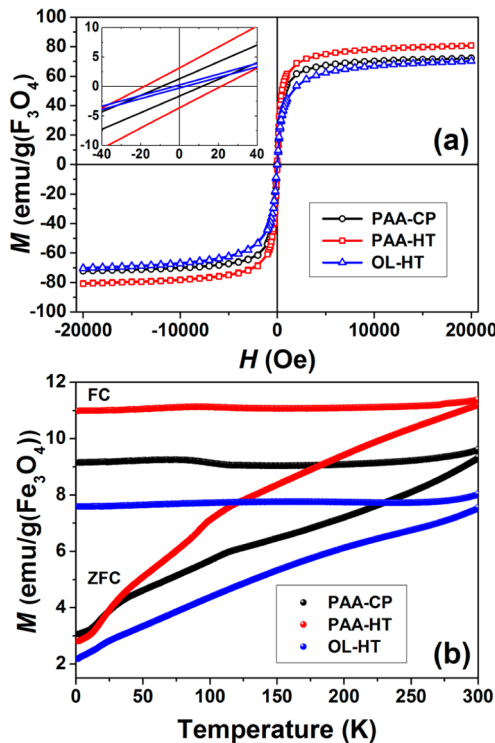


Figure 8. (a) Room temperature $M(H)$ dependence data for the synthesized NPs. The inset is an expanded view of the low-field region. (b) $M(T)$ dependence data for synthesized NPs measured at 100 Oe with use of ZFC (bottom curves) and FC (top curves) modes.

(Table 1) of our Fe_3O_4 NPs is indeed sufficiently large to produce interparticle magnetic interactions. The weak features below 125 K observed in Figure 8b can be assigned to the Verwey transition in Fe_3O_4 .³³

Hyperthermia. The hyperthermia performance of the three synthesized colloids was determined by using NP dispersions in water at concentration of 15 g/L, which is optimal for measurements in our hyperthermia apparatus. To produce aqueous dispersions of hydrophobic OL-HT NPs, we have carried out a phase transfer from organic to aqueous medium using a surfactant-assisted protocol from the literature.³⁴ In Figure 9, the temperature profiles are plotted as a function of time ($T(t)$); the corresponding SAR values are listed in Table 2. All colloids attained the therapeutically significant value of 316 K required to produce necrosis of cancer cells. Under the same experimental conditions, hydrothermally produced PAA-HT NPs outperformed PAA-CP and OL-HT NPs. Hyperthermia in PAA-HT NPs increased the temperature of the medium from 298 to 363 K ($\Delta T = 65$ K) after just 10 min of field exposure, whereas PAA-CP and OL-HT NPs heated the medium to 350 and 341 K (ΔT of 52 and 43 K, respectively).

4. DISCUSSION

Structure and Composition. We have successfully synthesized SPM Fe_3O_4 colloids composed of NPs with mean size between ca. 13 and 20 nm. Our spectroscopy and microscopy analyses of these NPs provide insight into a puzzling question regarding the structure and composition of SPM Fe_3O_4 NPs, namely, whether NPs have a distinct core–shell-like structure, such as $\text{Fe}_3\text{O}_4@\gamma\text{-Fe}_2\text{O}_3$, or a more smoothly varying nonstoichiometric $\text{Fe}_3\text{O}_{4+\delta}$ formulation.

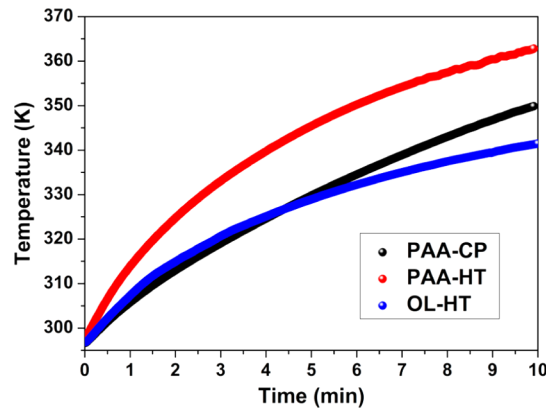


Figure 9. $T(t)$ profiles of NP-mediated magnetic hyperthermia for the colloidal dispersions of PAA-CP, PAA-HT, and OL-HT NPs. The measurements for all dispersions were conducted under the same conditions: 300 kHz frequency, 150 Oe field amplitude, and 15 g/L NP concentration in water.

The combination of phase-pure Fe_3O_4 composition indicated by XRD (Figure 4) and ED measurements, which are dominated by the inner volume of the NPs, and of $\gamma\text{-Fe}_2\text{O}_3$ signatures in the Raman spectra (Figure 5) of all the samples indicates that an overoxidized surface layer is present on all our NPs, which is consistent with previous reports for similar samples.^{13b,14a}

To estimate the surface oxide composition from XPS data, we use the areas of O 1s component that correspond to iron oxide (O–Fe in Figure 7) and of Fe 3p peak (data not shown) with the standard “atomic %” normalization; Fe 3p rather than Fe 2p peak area is used because the intensity of the former can be estimated with lower uncertainty. For PAA-coated samples PAA-CP and PAA-HT, the O/Fe ratio is approximately 2.4 ± 0.1 , which is above the stoichiometry of any iron oxide. This elevated O/Fe ratio indicates that a 2–3 nm surface layer of NPs probed by XPS is enriched with O, perhaps due to direct reactions of Fe with O-rich carboxylic groups of the organic shells and to the formation of $\text{Fe}_3\text{O}_4-\gamma\text{-Fe}_2\text{O}_3$ solid solutions at NP surfaces. This interpretation is supported by Fe 2p spectra (Figure 6), which indicate some enrichment of trivalent iron in the outermost (2–3 nm) surface of the NPs. As indicated earlier and briefly discussed in the SI, the analysis of O/Fe ratio for OL-HT is, unfortunately, rendered inconclusive by a dominant contribution from a sample preparation artifact (Figure S3, SI).

As HRTEM does not reveal any distinct core–shell nanostructuring of the particles, we hypothesize that as-prepared NPs have $\text{Fe}_3\text{O}_{4+\delta}$ composition and can be viewed as phase-pure magnetite with an outermost surface overoxidized to a varying extent. The overoxidized surface likely originates from topotactic oxidation of the reactive magnetite, resulting in the formation of $\text{Fe}_3\text{O}_4-\gamma\text{-Fe}_2\text{O}_3$ solid solution at the outermost NP surface.³⁵ Distinct core–shell nanostructure has been reported previously for colloidal SPM Fe_3O_4 NPs,^{9a,12,13} therefore, we conclude that an optimal preparation route for iron oxide NPs having core–shell vs more uniform internal structure should be carefully selected based on the specific intended applications.

Mechanism of Formation. Despite a relatively small amount of twinned and dimer Fe_3O_4 NPs observed by HRTEM in the hydrothermally synthesized samples, the influence of these defective NPs on the magnetic properties of a material is

not negligible.³⁶ Furthermore, the observation of the dimer and twinned NPs *only* in hydrothermally synthesized products provides insight into the mechanism of their formation.

Specifically, the presence of numerous structural defects in the hydrothermally synthesized NPs, as revealed by HRTEM and GPA images (Figures 2–3), suggests oriented-attachment³⁷ mechanism of formation for NPs with internal structural defects. Fe₃O₄ nanocrystals initially adhere to minimize their surface energy, adjusting to share a common crystallographic orientation; this local fusion is promoted by desorption of the capping ligands at the interface. The intergrowth of fused primary particles then leads to the formation of NPs with internal structural defects (Figure 2b). Their subsequent structural relaxation drives these NPs to adopt nearly spherical shapes (Figure 3a). During this structural relaxation, the stacking fault defect migrates to roughly the middle of the particle, hinting at a mass transport process via surface diffusion.³⁸ This rapid surface diffusion requires significant energy, which is available under hydrothermal but not under coprecipitation conditions, i.e., our hypothetical mechanism naturally accounts for observing defect NPs exclusively in the colloids produced under elevated temperatures in the presence of a surfactant.

Colloidal Stability. The stability of water-dispersible Fe₃O₄ NPs versus solution pH changes is consistent with the behavior expected for their PAA shells ($pK \approx 4.5$).³⁹ Both PAA-coated colloids are basic as-prepared, having pH values of approximately 9.5. After pH is reduced to 4, the colloids become unstable, agglomerate, and eventually precipitate; however, fresh precipitates can be redispersed by increasing pH. While this pH dependence of the colloidal stability indicates the importance of electrostatic stabilization, influence of additional factors is suggested by the concentration dependence of the colloidal stability. For instance, strong dilution of the PAA-coated colloids leads to irreversible aggregation of the NPs, as observed visually and by DLS.

Saturation Magnetization. A range of M_s values has been previously reported for colloidal SPM Fe₃O₄ NPs; those values diverge significantly and depend on the particle diameter and polydispersity, synthesis protocol, composition, and coating.^{7,9a,12,13} Our high M_s values are comparable to those of NPs with diameters ≥ 20 nm and are much higher than those reported for small NPs,^{6,40} leading us to consider the possible mechanisms for producing the high M_s values in our NPs.

Possible surface effects of capping ligands on the enhancement of M_s have been debated in the literature,^{7,16} however, we assume that such effects are not significant for NPs synthesized in this work. Specifically, the putative increased crystallinity induced by bonding of the organic ligands to the surface atoms⁷ of the iron oxide core is expected to be most significant for NPs with sizes ≤ 10 nm, in which a substantial fraction of the atoms is localized at the affected surface.⁴¹ Conversely, this effect would be much less significant in our ≥ 13 nm NPs. Another effect proposed for surface-functionalized magnetite NPs relies on adsorbed surfactant molecules affecting the ferromagnetic coupling of iron atoms. The maximum number of adsorbed surfactant molecules on the surface of our relatively large (13–20 nm) NPs, however, is too small to play a decisive role in the magnetic properties. Any putative ordering effect of the organic ligands would need to extend below the NP surface to affect the M_s . For example, a surface composed of one ordered layer of FeO₆ octahedra would have only a weak impact on the M_s . To significantly influence the M_s , the ligand-mediated restructuring

of the NP surface layer would have to extend below ≥ 1 nm, but we did not observe evidence of such extensive surface layer restructuring in HRTEM/GPA studies.

The high M_s of our SPM NPs, approaching that of bulk magnetite (98 emu/g), could hypothetically be related to the presence of single-domain FiM NPs (30–90 nm) in the synthesized magnetite samples. Our TEM data, however, do not support this impurity interpretation: we did not observe a single NP with a diameter > 50 nm in any of our TEM images and even NPs with diameters around 30 nm are exceedingly rare.

Having rejected the surface effect and large-NP-impurity possibilities, we believe that the large particle diameter (13–20 nm) and elevated temperatures of the synthesis (363, 473 K) are the major factors accounting for the high M_s values of our products.

Magnetic hyperthermia is a good example of an application of SPM Fe₃O₄ NPs in which high M_s values provide a significant advantage. Our hyperthermia results (Table 2) indicate a qualitative correlation between SAR and M_s values of the samples, in agreement with the Rosensweig model.¹⁸ Accordingly, our colloidal PAA-HT NPs that exhibited the highest M_s values also demonstrated the most efficient heating ability.

5. CONCLUSIONS

In summary, colloidal Fe₃O₄ NPs have been successfully prepared in large quantities using novel or improved methods based on controlled coprecipitation and hydrothermal synthesis. Physical property measurements reveal that our strategy for increasing the size of the particles toward 20 nm through synthesis under elevated temperatures has worked effectively, offering functional SPM Fe₃O₄ NPs with the desired exceptionally high M_s . Our comprehensive structural and compositional analysis reveals that the synthesized NPs are phase-pure magnetite with an overoxidized outermost surface, and do not exhibit a putative distinct Fe₃O₄@ γ -Fe₂O₃ core–shell structure. Unprecedented details about the fine microstructure of the synthesized NPs have been established by TEM coupled with geometric phase analysis. In particular, we find defect nanoparticles that form under the hydrothermal conditions via oriented attachment crystal growth, whereby two magnetite nanocrystals initially join together and interact, followed by cogrowing as a single defective NP. We also explored nanoparticle-mediated magnetic hyperthermia performance of the synthesized NPs; our results are in agreement with hyperthermia models that predict a correlation between the heating ability and saturation magnetization of SPM NPs.

■ ASSOCIATED CONTENT

● Supporting Information

A detailed description of characterization techniques, as well as additional synthesis, Raman scattering, XPS, TGA-DSC-MS, and colloidal stability data. This material is available free of charge via the Internet at <http://pubs.acs.org>.

■ AUTHOR INFORMATION

Corresponding Author

*E-mail: yury.kolenko@inl.int.

Notes

The authors declare no competing financial interest.

ACKNOWLEDGMENTS

We thank Dr. Albert Ng for his help with XPS analysis, and Prof. P. Freitas, Prof. M. A. López-Quintela, Dr. T. J. La Tempa, and Dr. L. M. Salonen for helpful discussions. The authors acknowledge the European Regional Development Fund (ON.2 - O Novo Norte Program), EU FP7 Cooperation Program through NMP-theme (Grant no. 314212), Xunta de Galicia, Spain (Grant no. 2010/PX168), and InveNNta project financed by EU Programme for Cross-border Cooperation: Spain-Portugal (POCTEP 2007–2013) for support of this work. E.C.-A. acknowledges the I2C Plan (Xunta de Galicia, Spain) for a postdoctoral Fellowship.

REFERENCES

- (1) Cornell, R. M.; Schwertmann, U. *The Iron Oxides: Structure, Properties, Reactions, Occurrences and Uses*; Wiley-VCH: Weinheim, Germany, 2003.
- (2) Krishnan, K. M. Biomedical Nanomagnetics: A Spin Through Possibilities in Imaging, Diagnostics, and Therapy. *IEEE Trans. Magn.* **2010**, *46*, 2523–2558.
- (3) Corot, C.; Robert, P.; Idee, J. M.; Port, M. Recent Advances in Iron Oxide Nanocrystal Technology for Medical Imaging. *Adv. Drug Delivery Rev.* **2006**, *58*, 1471–1504.
- (4) Muldoon, L. L.; Sandor, M.; Pinkston, K. E.; Neuwelt, E. A. Imaging, Distribution, and Toxicity of Superparamagnetic Iron Oxide Magnetic Resonance Nanoparticles in the Rat Brain and Intracerebral Tumor. *Neurosurgery* **2005**, *57*, 785–796.
- (5) (a) Gao, J. H.; Gu, H. W.; Xu, B. Multifunctional Magnetic Nanoparticles: Design, Synthesis, and Biomedical Applications. *Acc. Chem. Res.* **2009**, *42*, 1097–1107. (b) Shylesh, S.; Schunemann, V.; Thiel, W. R. Magnetically Separable Nanocatalysts: Bridges between Homogeneous and Heterogeneous Catalysis. *Angew. Chem. Int. Ed.* **2010**, *49*, 3428–3459. (c) Jung, J. H.; Lee, J. H.; Shinkai, S. Functionalized Magnetic Nanoparticles as Chemosensors and Adsorbents for Toxic Metal Ions in Environmental and Biological Fields. *Chem. Soc. Rev.* **2011**, *40*, 4464–4474. (d) Ling, M. M.; Wang, K. Y.; Chung, T. S. Highly Water-Soluble Magnetic Nanoparticles as Novel Draw Solutes in Forward Osmosis for Water Reuse. *Ind. Eng. Chem. Res.* **2010**, *49*, 5869–5876.
- (6) (a) Koseoglu, Y. Effect of Surfactant Coating on Magnetic Properties of Fe_3O_4 Nanoparticles: ESR Study. *J. Magn. Magn. Mater.* **2006**, *300*, E327–E330. (b) Laurent, S.; Forge, D.; Port, M.; Roch, A.; Robic, C.; Elst, L. V.; Muller, R. N. Magnetic Iron Oxide Nanoparticles: Synthesis, Stabilization, Vectorization, Physicochemical Characterizations, and Biological Applications. *Chem. Rev.* **2008**, *108*, 2064–2110.
- (7) Guardia, P.; Labarta, A.; Batlle, X. Tuning the Size, the Shape, and the Magnetic Properties of Iron Oxide Nanoparticles. *J. Phys. Chem. C* **2011**, *115*, 390–396.
- (8) (a) Jolivet, J. P.; Chaneac, C.; Tronc, E. Iron Oxide Chemistry. From Molecular Clusters to Extended Solid Networks. *Chem. Commun.* **2004**, 481–487. (b) Vayssières, L.; Chaneac, C.; Tronc, E.; Jolivet, J. P. Size Tailoring of Magnetite Particles Formed by Aqueous Precipitation: An Example of Thermodynamic Stability of Nanometric Oxide Particles. *J. Colloid Interface Sci.* **1998**, *205*, 205–212.
- (9) (a) Park, J.; An, K. J.; Hwang, Y. S.; Park, J. G.; Noh, H. J.; Kim, J. Y.; Park, J. H.; Hwang, N. M.; Hyeon, T. Ultra-large-scale Syntheses of Monodisperse Nanocrystals. *Nat. Mater.* **2004**, *3*, 891–895. (b) Sun, S. H.; Zeng, H.; Robinson, D. B.; Raoux, S.; Rice, P. M.; Wang, S. X.; Li, G. X. Monodisperse MFe_2O_4 ($\text{M} = \text{Fe}, \text{Co}, \text{Mn}$) Nanoparticles. *J. Am. Chem. Soc.* **2004**, *126*, 273–279.
- (10) Verges, M. A.; Costo, R.; Roca, A. G.; Marco, J. F.; Goya, G. F.; Serna, C. J.; Morales, M. P. Uniform and Water Stable Magnetite Nanoparticles with Diameters around the Monodomain-multidomain Limit. *J. Phys. D: Appl. Phys.* **2008**, *41*, 134003.
- (11) Ditsch, A.; Laibinis, P. E.; Wang, D. I. C.; Hatton, T. A. Controlled Clustering and Enhanced Stability of Polymer-coated Magnetic Nanoparticles. *Langmuir* **2005**, *21*, 6006–6018.
- (12) Salazar, J. S.; Perez, L.; de Abril, O.; Lai, T. P.; Ihiawakrim, D.; Vazquez, M.; Greneche, J. M.; Begin-Colin, S.; Pourroy, G. Magnetic Iron Oxide Nanoparticles in 10–40 nm Range: Composition in Terms of Magnetite/Maghemite Ratio and Effect on the Magnetic Properties. *Chem. Mater.* **2011**, *23*, 1379–1386.
- (13) (a) Daou, T. J.; Pourroy, G.; Begin-Colin, S.; Greneche, J. M.; Ulhaq-Bouillet, C.; Legare, P.; Bernhardt, P.; Leuvrey, C.; Rogez, G. Hydrothermal Synthesis of Monodisperse Magnetite Nanoparticles. *Chem. Mater.* **2006**, *18*, 4399–4404. (b) Tang, J.; Myers, M.; Bosnick, K. A.; Brus, L. E. Magnetite Fe_3O_4 Nanocrystals: Spectroscopic Observation of Aqueous Oxidation Kinetics. *J. Phys. Chem. B* **2003**, *107*, 7501–7506. (c) Goss, C. J. Saturation Magnetization, Coercivity and Lattice-Parameter Changes in the System Fe_3O_4 -gamma- Fe_2O_3 , and Their Relationship to Structure. *Phys. Chem. Miner.* **1988**, *16*, 164–171.
- (14) (a) Taniguchi, T.; Nakagawa, K.; Watanabe, T.; Matsushita, N.; Yoshimura, M. Hydrothermal Growth of Fatty Acid Stabilized Iron Oxide Nanocrystals. *J. Phys. Chem. C* **2009**, *113*, 839–843. (b) Wouters, J.; Lebedev, O. I.; Van Tendeloo, G.; Yamada, H.; Sato, N.; Vanacken, J.; Moshchalkov, V. V.; Verbiest, T.; Valev, V. K. Preparing Polymer Films Doped with Magnetic Nanoparticles by Spin-coating and Melt-processing Can Induce an In-plane Magnetic Anisotropy. *J. Appl. Phys.* **2011**, *109*, 076105.
- (15) (a) Schmidbauer, E.; Keller, M. Magnetic Hysteresis Properties, Mössbauer Spectra and Structural Data of Spherical 250 nm Particles of Solid Solutions Fe_3O_4 -gamma- Fe_2O_3 . *J. Magn. Magn. Mater.* **2006**, *297*, 107–117. (b) Weber, H. P.; Hafner, S. S. Vacancy Distribution in Nonstoichiometric Magnetites. *Z. Kristallogr.* **1971**, *133*, 327–340.
- (16) Guardia, P.; Batlle-Brugal, B.; Roca, A. G.; Iglesias, O.; Morales, M. P.; Serna, C. J.; Labarta, A.; Batlle, X. Surfactant Effects in Magnetite Nanoparticles of Controlled Size. *J. Magn. Magn. Mater.* **2007**, *316*, E756–E759.
- (17) Johannsen, M.; Gneveckow, U.; Eckelt, L.; Feussner, A.; Waldofner, N.; Scholz, R.; Deger, S.; Wust, P.; Loening, S. A.; Jordan, A. Clinical Hyperthermia of Prostate Cancer Using Magnetic Nanoparticles: Presentation of a New Interstitial Technique. *Int. J. Hyperthermia* **2005**, *21*, 637–647.
- (18) Rosensweig, R. E. Heating Magnetic Fluid with Alternating Magnetic Field. *J. Magn. Magn. Mater.* **2002**, *252*, 370–374.
- (19) Carrey, J.; Mehdaoui, B.; Respaud, M. Simple Models for Dynamic Hysteresis Loop Calculations of Magnetic Single-Domain Nanoparticles: Application to Magnetic Hyperthermia Optimization. *J. Appl. Phys.* **2011**, *109*, 083921.
- (20) Vallejo-Fernandez, G.; Whear, O.; Roca, A. G.; Hussain, S.; Timmis, J.; Patel, V.; O'Grady, K. Mechanisms of Hyperthermia in Magnetic Nanoparticles. *J. Phys. D: Appl. Phys.* **2013**, *46*, 312001.
- (21) (a) Grazulis, S.; Chateigner, D.; Downs, R. T.; Yokochi, A. F. T.; Quirós, M.; Lutterotti, L.; Manakova, E.; Butkus, J.; Moeck, P.; Le Bail, A. Crystallography Open Database - an Open-access Collection of Crystal Structures. *J. Appl. Crystallogr.* **2009**, *42*, 726–729. (b) Akselrud, L. G.; Zavalii, P. Y.; Grin, Y. N.; Pecharsky, V. K.; Baumgartner, B.; Wolfel, E. Use of the CSD Program Package for Structure Determination from Powder Data. *Mater. Sci. Forum* **1993**, *133–136*, 335–340.
- (22) (a) Seah, M. P.; Gilmore, L. S.; Beamson, G. XPS: Binding Energy Calibration of Electron Spectrometers 5 - Re-evaluation of the Reference Energies. *Surf. Interface Anal.* **1998**, *26*, 642–649. (b) Petrovykh, D. Y.; Kimura-Suda, H.; Opdahl, A.; Richter, L. J.; Tarlov, M. J.; Whitman, L. J. Alkanethiols on Platinum: Multi-component Self-assembled Monolayers. *Langmuir* **2006**, *22*, 2578–2587. (c) Scofield, J. H. Hartree-Slater Subshell Photoionization Cross-Sections at 1254 and 1487 eV. *J. Electron Spectrosc. Relat. Phenom.* **1976**, *8*, 129–137. (d) Jablonski, A.; Powell, C. J. The Electron Attenuation Length Revisited. *Surf. Sci. Rep.* **2002**, *47*, 35–91.

- (23) Hytch, M. J.; Snoeck, E.; Kilaas, R. Quantitative Measurement of Displacement and Strain Fields from HREM Micrographs. *Ultramicroscopy* **1998**, *74*, 131–146.
- (24) Hong, J. H.; Kim, W. S.; Lee, J. I.; Hur, N. H. Exchange Coupled Magnetic Nanocomposites of $\text{Sm}(\text{Co}_{1-x}\text{Fe}_x)_5/\text{Fe}_3\text{O}_4$ with Core/Shell Structure. *Solid State Commun.* **2007**, *141*, 541–544.
- (25) (a) Shebanova, O. N.; Lazor, P. Raman Spectroscopic Study of Magnetite (FeFe_2O_4): a New Assignment for the Vibrational Spectrum. *J. Solid State Chem.* **2003**, *174*, 424–430. (b) Jubb, A. M.; Allen, H. C. Vibrational Spectroscopic Characterization of Hematite, Maghemite, and Magnetite Thin Films Produced by Vapor Deposition. *ACS Appl. Mater. Interfaces* **2010**, *2*, 2804–2812.
- (26) (a) Grosvenor, A. P.; Kobe, B. A.; McIntyre, N. S.; Tougaard, S.; Lennard, W. N. Use of QUASES/XPS Measurements to Determine the Oxide Composition and Thickness on an Iron Substrate. *Surf. Interface Anal.* **2004**, *36*, 632–639. (b) Hawn, D. D.; DeKoven, B. M. Deconvolution as a Correction for Photoelectron Inelastic Energy Losses in the Core Level XPS Spectra of Iron Oxides. *Surf. Interface Anal.* **1987**, *10*, 63–74.
- (27) (a) Jung, C. W. Surface-Properties of Superparamagnetic Iron-Oxide MR Contrast Agents - Ferumoxides, Ferumoxtran, Ferumoxsil. *Magn. Reson. Imaging* **1995**, *13*, 675–691. (b) Mondini, S.; Cenedese, S.; Marinoni, G.; Molteni, G.; Santo, N.; Bianchi, C. L.; Ponti, A. One-step Synthesis and Functionalization of Hydroxyl-decorated Magnetite Nanoparticles. *J. Colloid Interface Sci.* **2008**, *322*, 173–179.
- (28) (a) Fujii, T.; de Groot, F. M. F.; Sawatzky, G. A.; Voogt, F. C.; Hibma, T.; Okada, K. In Situ XPS Analysis of Various Iron Oxide Films Grown by NO_2 -assisted Molecular-beam Epitaxy. *Phys. Rev. B* **1999**, *59*, 3195–3202. (b) Kendelewicz, T.; Liu, P.; Doyle, C. S.; Brown, G. E., Jr.; Nelson, E. J.; Chambers, S. A. Reaction of water with the (100) and (111) surfaces of Fe_3O_4 . *Surf. Sci.* **2000**, *453*, 32–46. (c) Ruby, C.; Humbert, B.; Fusy, J. Surface and Interface Properties of Epitaxial Iron Oxide Thin Films Deposited on $\text{MgO}(001)$ Studied by XPS and Raman Spectroscopy. *Surf. Interface Anal.* **2000**, *29*, 377–380.
- (29) Lock, E. H.; Petrovykh, D. Y.; Mack, P.; Carney, T.; White, R. G.; Walton, S. G.; Fernsler, R. F. Surface Composition, Chemistry, and Structure of Polystyrene Modified by Electron-Beam-Generated Plasma. *Langmuir* **2010**, *26*, 8857–8868.
- (30) Maity, D.; Choo, S.-G.; Yi, J.; Ding, J.; Xue, J. M. Synthesis of Magnetite Nanoparticles Via a Solvent-free Thermal Decomposition Route. *J. Magn. Magn. Mater.* **2009**, *321*, 1256–1259.
- (31) Vazquez-Vazquez, C.; Lopez-Quintela, M. A.; Bujan-Nunez, M. C.; Rivas, J. Finite Size and Surface Effects on the Magnetic Properties of Cobalt Ferrite Nanoparticles. *J. Nanopart. Res.* **2011**, *13*, 1663–1676.
- (32) Kallumadil, M.; Tada, M.; Nakagawa, T.; Abe, M.; Southern, P.; Pankhurst, Q. A. Suitability of commercial colloids for magnetic hyperthermia. *J. Magn. Magn. Mater.* **2009**, *321*, 1509–1513.
- (33) Verwey, E. J. W. Electronic Conduction of Magnetite (Fe_3O_4) and Its Transition Point at Low Temperatures. *Nature* **1939**, *144*, 327–328.
- (34) Salgueirino-Maceira, V.; Correa-Duarte, M. A.; Farle, M. Manipulation of Chemically Synthesized FePt Nanoparticles in Water: Core-shell Silica/FePt Nanocomposites. *Small* **2005**, *1*, 1073–1076.
- (35) (a) Gorski, C. A.; Scherer, M. M. Determination of Nanoparticulate Magnetite Stoichiometry by Mössbauer Spectroscopy, Acidic Dissolution, and Powder X-ray Diffraction: A Critical Review. *Am. Mineral.* **2010**, *95*, 1017–1026. (b) Frison, R.; Cernuto, G.; Cervellino, A.; Zaharko, O.; Colonna, G. M.; Guagliardi, A.; Masciocchi, N. Magnetite–Maghemite Nanoparticles in the 5–15 nm Range: Correlating the Core–Shell Composition and the Surface Structure to the Magnetic Properties. A Total Scattering Study. *Chem. Mater.* **2013**, *25*, 4820–4827.
- (36) Ray, S.; Kolen'ko, Y. V.; Kovnir, K. A.; Lebedev, O. I.; Turner, S.; Chakraborty, T.; Erni, R.; Watanabe, T.; Van Tendeloo, G.; Yoshimura, M.; Itoh, M. Defect Controlled Room Temperature Ferromagnetism in Co-doped Barium Titanate Nanocrystals. *Nanotechnology* **2012**, *23*, 025702.
- (37) Penn, R. L.; Banfield, J. F. Imperfect Oriented Attachment: Dislocation Generation in Defect-free Nanocrystals. *Science* **1998**, *281*, 969–971.
- (38) Mullins, W. W. Theory of Thermal Grooving. *J. Appl. Phys.* **1957**, *28*, 333–339.
- (39) Lattuada, M.; Hatton, T. A. Functionalization of Monodisperse Magnetic Nanoparticles. *Langmuir* **2007**, *23*, 2158–2168.
- (40) Gnanaprakash, G.; Philip, J.; Jayakumar, T.; Raj, B. Effect of Digestion Time and Alkali Addition Rate on Physical Properties of Magnetite Nanoparticles. *J. Phys. Chem. B* **2007**, *111*, 7978–7986.
- (41) Auffan, M.; Rose, J.; Bottero, J. Y.; Lowry, G. V.; Jolivet, J. P.; Wiesner, M. R. Towards a Definition of Inorganic Nanoparticles from an Environmental, Health and Safety Perspective. *Nat. Nanotechnol.* **2009**, *4*, 634–641.